First-principles study of the electrical resistivity in zirconium dichalcogenides with multivalley bands: Mode-resolved analysis of electron-phonon scattering

Hitoshi Mori⊙, Masayuki Ochi⊙, and Kazuhiko Kuroki

Department of Physics, Osaka University, Machikaneyama-cho, Toyonaka, Osaka 560-0043, Japan

Based on first-principles calculations, we study the electron-phonon scattering effect on the resistivity in the zirconium dichalcogenides, ZrS_2 and $ZrSe_2$, whose electronic band structures possess multiple valleys at the conduction band minimum. The computed resistivity exhibits nonlinear temperature dependence, especially for ZrS_2, which is also experimentally observed on some transition metal dichalcogenides such as TiS_2 and $ZrSe_2$. By performing the decomposition of the contributions of scattering processes, we find that the intravalley scattering by acoustic phonons mainly contributes to the resistivity around 50 K. Moreover, the contribution of the intravalley scattering by optical phonons becomes dominant even above 80 K, which is a sufficiently low temperature compared with their frequencies. By contrast, the effect of the intervalley scattering is found to be not significant. Our study identifies the characteristic scattering channels in the resistivity of the zirconium dichalcogenides, which provides critical knowledge to microscopically understand electron transport in systems with multivalley band structure.

I. INTRODUCTION

Transition metal dichalcogenides (TMDCs) [1–4] are layered materials of the form MX_2, where M and X are transition metal and chalcogen atoms, respectively. The TMDCs have been extensively investigated due to a wide range of physical properties and potential applications originating from the unique band structures, such as superconductivity [5–9], magnetic ordering [10–13], charge density waves (CDWs) [14–23], exciton dynamics [24–30], topological semimetal states [31–41], and thermoelectricity [42–51]. In some typical TMDCs, the electronic band structure shows multiple valleys around the Fermi level, where a valley implies a local extremum of the band structure; the manipulation of the valley degree of freedom has attracted considerable attention for valleytronics applications [52–64]. In addition, the effect of scattering between valleys, namely, intervalley scattering, have been investigated from various perspectives such as excitonic electron-hole exchange interaction [24–26,30], CDW instability [14–18,22], and electrical transport [42,44,65–73].

The effect of intervalley scattering is also considered to be a key factor in the thermoelectric performance [74–77]. Higher valley degeneracy leads to higher carrier density but, at the same time, results in a higher possibility of electron scattering, which in turn suppresses the electrical conductivity. In particular, it has been argued that intervalley scattering induced by acoustic phonons strongly affects the electrical transport in addition to intravalley scattering by acoustic phonons, and it may cause the quadraticlike temperature dependence of electrical resistivity of TiS_2 observed over a wide temperature range [42,44,68,73]. The quadraticlike temperature dependence has been observed not only in TiS_2 [42,44,65–69,73,78–80]

but also in some other TMDCs such as $ZrSe_2$ [69–71], $HfSe_2$ [70], and $MoTe_2$ [72], and the electron scattering mechanism is still controversial. Other than intervalley scattering by acoustic phonons, some other scattering mechanisms such as optical phonon scattering [69,70,78–81], electron-electron scattering [67,82], electron-hole scattering [80,82,83], and ionized impurity scattering [71] have also been proposed as crucial mechanisms determining the transport properties. Although some first-principles studies of the intervalley scattering effect in some TMDCs and other materials have recently been performed in terms of electron-phonon scattering [84–88], they have not pursued the cause of the quadratic temperature dependence of resistivity. Elucidating the origin of the temperature dependence will lead to acquiring knowledge essential for controlling transport properties such as thermoelectric performance.

Given this background, in this paper, we theoretically investigate the electron-phonon scattering effect on the resistivity in the zirconium dichalcogenides, ZrS_2 and $ZrSe_2$, by means of first-principles calculations. The theoretical approach employed in this paper can take into account the electron-phonon scattering by all the phonon modes. We shall show that the intravalley scattering is a dominant contributor to the resistivity in a wide temperature range and that the contribution from the intravalley scattering by optical phonons increases with increasing temperature. Our detailed analysis unambiguously identifies the phonon states which strongly scatter the electrons and thus dominantly contribute to the resistivity at both low and high temperatures, 50 and 300 K. Based on these results, we reveal that the intravalley scattering caused by optical phonons is a primary factor in making the temperature dependence of resistivity nonlinear. We also conclude that the electrical resistivity of $ZrSe_2$ exhibits a

temperature dependence that is closer to linear than that of ZrS_2 because the frequencies of optical phonons of $ZrSe_2$ are lower.

The paper is organized as follows: In Sec. II we show the details of the calculation methods we used in this paper. Sections III A and III B present calculation results for ZrS_2 and $ZrSe_2$, respectively. We discuss the nonlinear temperature dependence of the resistivity in ZrS_2 in Sec. III A and the difference in the temperature dependence between ZrS_2 and $ZrSe_2$ in Sec. III B. Finally, a summary of the present study is presented in Sec. IV.

II. METHODS OF CALCULATIONS

All the first-principles calculations were performed using the QUANTUM ESPRESSO package [89–91] (version 6.3). Perdew-Burke-Ernzerhof parametrization adapted for solids of the generalized gradient approximation (PBEsol-GGA) [92,93] was used. Spin-orbit coupling was not included in the calculations. First, we determined the crystal structures through structural optimization, and then we performed the band-structure calculations. We used the optimized norm-conserving Vanderbilt (ONCV) pseudopotentials [94] extracted from the PSEUDODOJO library [95] and an $18 \times 18 \times 12$ $\boldsymbol{k}$ mesh for both materials. The plane-wave cutoff was set as 100 Ry. After the band-structure calculations, we performed phonon calculations within the density-functional perturbation theory (DFPT) on a $6 \times 6 \times 4$ $\boldsymbol{q}$-mesh sampling. Hereafter, the vector $\boldsymbol{k}$ implies the electronic wave-number vector, and the vector $\boldsymbol{q}$ is the phonon wave-number vector in this paper. In order to construct the effective models by using the maximally localized Wannier functions [96] and obtain the electron-phonon matrix elements on ultrafine $\boldsymbol{k}$ and $\boldsymbol{q}$ grids, we employed the EPW code [97–100] (version 5.2) of the QUANTUM ESPRESSO distribution, which is in conjunction with the WANNIER90 library [101–104] (version 3.0). We chose Zr s and S (Se) p orbitals as initial guesses for the Wannier functions and constructed 11-orbital effective models using a $12 \times 12 \times 8$ $\boldsymbol{k}$-mesh sampling. We interpolated the electron-phonon matrix elements to $96 \times 96 \times 72$ $\boldsymbol{k}$ and $\boldsymbol{q}$ grids to calculate the resistivity. Indeed, as for the $\boldsymbol{k}$ grid, only the 57,109 $\boldsymbol{k}$ points in the irreducible wedge were used. In this paper, we focus on the in-plane resistivity of both materials. For this purpose, we calculated the electrical conductivity tensor by the Boltzmann transport equation within the relaxation time approximation (RTA) as follows:

$$\boldsymbol{\sigma} = 2 \times \frac{e^2}{\Omega} \sum_{\boldsymbol{k},n} \tau_{\boldsymbol{k}n} \boldsymbol{v}_{\boldsymbol{k}n} \otimes \boldsymbol{v}_{\boldsymbol{k}n} \left(-\frac{\partial f_{\boldsymbol{k}n}}{\partial \varepsilon} \right) \tag{1}$$

with the Fermi-Dirac distribution function

$$f_{\boldsymbol{k}n} = \frac{1}{e^{\beta(\varepsilon_{\boldsymbol{k}n} - \mu)} + 1}. \tag{2}$$

The factor 2 at the head of the right-hand side of Eq. (1) comes from spin degeneracy. Ω is the volume of the crystal, e (>0) is the elementary charge, β is the inverse temperature defined as $\beta = (k_B T)^{-1}$ with the Boltzmann constant k_B, and μ is the Fermi level. $\tau_{\boldsymbol{k}n}$, $\varepsilon_{\boldsymbol{k}n}$, and $\boldsymbol{v}_{\boldsymbol{k}n}$ are the relaxation time, the energy level of the electron, and the group velocity on the nth

band at a certain $\boldsymbol{k}$ point, respectively. Here, the Fermi level μ was determined so as to provide a fixed electron carrier density of 1.0×10^{20} cm^{-3} for each temperature. The in-plane electrical resistivity was obtained by taking the inverse of the corresponding diagonal component of the electrical conductivity tensor $\boldsymbol{\sigma}$. In this paper, we compute the scattering rate, which is the inverse of the relaxation time, by using the following equation:

$$\frac{1}{\tau_{\boldsymbol{k}n}} = \frac{2\pi}{N_p \hbar} \sum_{\boldsymbol{q},\nu} \sum_{n'} |g_{n'n\nu}(\boldsymbol{k}, \boldsymbol{q})|^2$$
$$\times \left[W_{n'n\nu}^{(-)}(\boldsymbol{k}, \boldsymbol{q}) + W_{n'n\nu}^{(+)}(\boldsymbol{k}, \boldsymbol{q}) \right] \tag{3}$$

with

$$W_{n'n\nu}^{(\pm)}(\boldsymbol{k}, \boldsymbol{q}) = \begin{Bmatrix} f_{\boldsymbol{k}+\boldsymbol{q}n'} + n_{\boldsymbol{q}\nu} \\ 1 - f_{\boldsymbol{k}+\boldsymbol{q}n'} + n_{\boldsymbol{q}\nu} \end{Bmatrix} \delta(\varepsilon_{\boldsymbol{k}n} - \varepsilon_{\boldsymbol{k}+\boldsymbol{q}n'} \pm \hbar\omega_{\boldsymbol{q}\nu}),$$
$$\tag{4}$$

where N_p is the total number of $\boldsymbol{q}$ points in the first Brillouin zone, $n_{\boldsymbol{q}\nu} = (e^{\beta\hbar\omega_{\boldsymbol{q}\nu}} - 1)^{-1}$ is the Bose-Einstein distribution function, and $\omega_{\boldsymbol{q}\nu}$ is the frequency of the phonon on the νth phonon branch at a certain $\boldsymbol{q}$ point. $g_{n'n\nu}(\boldsymbol{k}, \boldsymbol{q})$ is the electron-phonon matrix element, which represents the scattering from the initial electronic state $|\boldsymbol{k}n\rangle$ to the final state $|\boldsymbol{k} + \boldsymbol{q}n'\rangle$ via a phonon in the state $(\boldsymbol{q}, \nu)$. We have confirmed that the size of the $\boldsymbol{k}$ and $\boldsymbol{q}$ grids adopted in this paper, $96 \times 96 \times 72$, is large enough to achieve the convergence for the electrical resistivity as presented in Appendix B 2. Equation (3) coincides with the expression of the scattering rate given by Fermi's golden rule [105–107].

III. RESULTS AND DISCUSSION

A. ZrS_2

Figure 1 presents the calculated electron and phonon band structures of ZrS_2. As shown in Fig. 1(a), the band structure of the effective model well reproduces the band structure obtained with first-principles calculations. Since n-type conductor behavior has been experimentally reported in related materials, TiS_2 [42,44,68,73] and $ZrSe_2$ [69–71], we focus on the transport properties of electron-doped ZrS_2 in this paper. As shown in Fig. 1(c), there exist three Fermi pockets of electrons in the first Brillouin zone. The schematic illustration of Fermi surfaces is shown in Fig. 1(d). We note that the Fermi pockets are situated around the L points, and the scattering between the states on different pockets is the intervalley scattering.

Figure 2 presents the calculated electron-phonon matrix elements, where the Wannier-interpolated ones and those explicitly obtained by DFPT calculations are shown by blue dots and black squares, respectively. It is seen that the $\boldsymbol{q}$ dependence of the interpolated electron-phonon matrix elements well reproduces the dependence obtained from DFPT calculations on most $\boldsymbol{q}$ paths. However, for some $\boldsymbol{q}$ points along the Γ-A line, the interpolated electron-phonon matrix elements are larger than the ones obtained from DFPT calculations. This is due to the fact that the interpolation is not completely
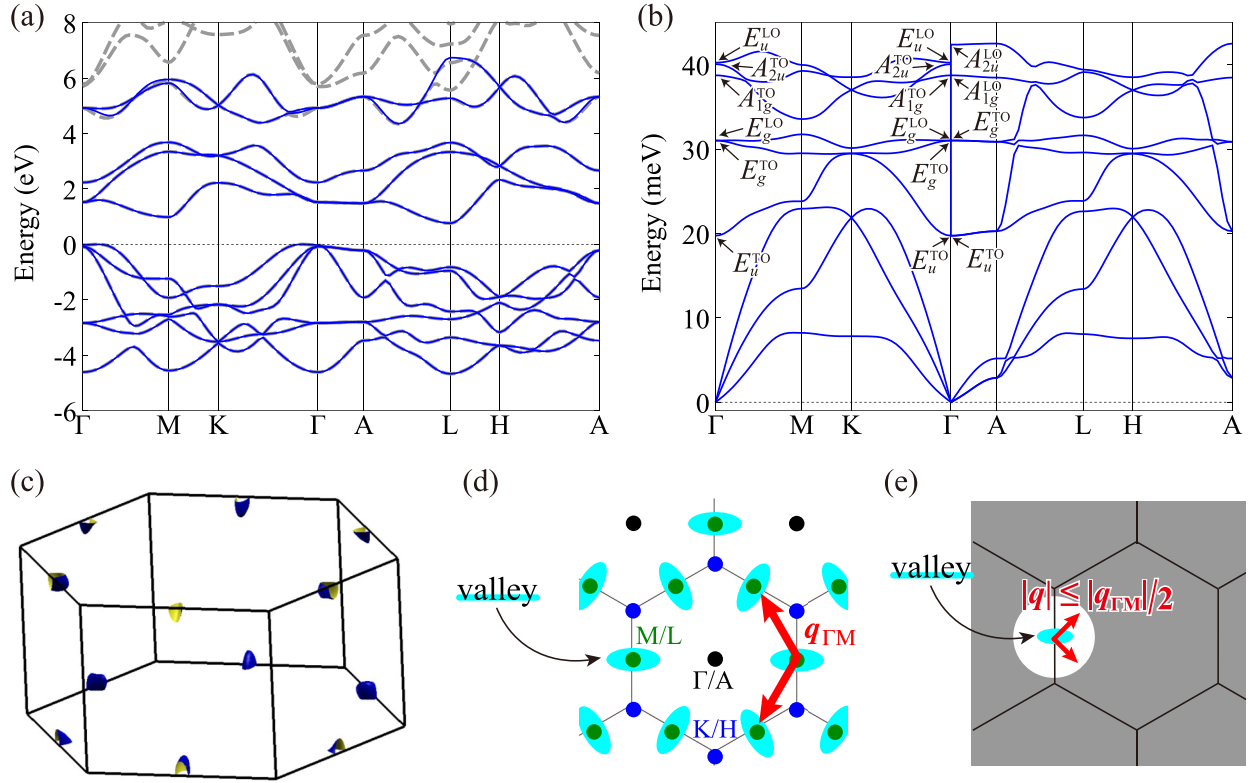
FIG. 1. (a) Electronic band structures of ZrS_2 obtained from first-principles calculation (dashed gray lines) and the effective model constructed by Wannier orbitals (solid blue lines). (b) The phonon dispersion. The optical modes in the long-wavelength limit are specified by Mulliken symbols [108]. (c) The Fermi surface for the electron carrier density of 1.0×10^{20} cm^{-3} at 300 K, which was plotted with XCRYSDEN software [109]. (d) Schematic illustration of the Fermi surfaces in the Brillouin zone. The red arrows correspond to the scattering vectors. (e) Illustration of the condition $|q| \leqslant |q_{\Gamma M}|/2$, which is used to sum over wave vectors q only corresponding to intravalley scattering vectors.

successful. We have confirmed that this difference has little effect on the electrical resistivity. (See Appendix B 1.) We note that discontinuous jumps in Fig. 2 come from switchings between phonon branches at their crossing points. As can be seen in Fig. 2(d), the electron-phonon matrix elements diverge in the long-wavelength limit $q \to 0$ because the corresponding coupling indicates that electrons couple with longitudinal optical (LO) phonons inducing macroscopic fields.

1. Temperature dependence of the electrical resistivity

From the interpolated electron-phonon matrix elements, we calculated the scattering rate and the electrical resistivity. To clarify which phonons mainly scatter electrons and whether intravalley scattering or intervalley scattering plays a significant role in the resistivity, we decomposed the scattering rate in terms of the q-space region and the phonon branches as follows:

$$\frac{1}{\tau_{kn}^{(\text{intra-ac})}} = \frac{2\pi}{N_p \hbar} \sum_{|q| \leqslant |q_{\Gamma M}|/2} \sum_{\nu=1}^{3} \sum_{n'} |g_{n'n\nu}(k, q)|^2 \big[W_{n'n\nu}^{(-)}(k, q) + W_{n'n\nu}^{(+)}(k, q) \big], \tag{5}$$

$$\frac{1}{\tau_{kn}^{(\text{intra-op})}} = \frac{2\pi}{N_p \hbar} \sum_{|q| \leqslant |q_{\Gamma M}|/2} \sum_{\nu=4}^{9} \sum_{n'} |g_{n'n\nu}(k, q)|^2 \big[W_{n'n\nu}^{(-)}(k, q) + W_{n'n\nu}^{(+)}(k, q) \big], \tag{6}$$

$$\frac{1}{\tau_{kn}^{(\text{inter-ac})}} = \frac{2\pi}{N_p \hbar} \sum_{|q| > |q_{\Gamma M}|/2} \sum_{\nu=1}^{3} \sum_{n'} |g_{n'n\nu}(k, q)|^2 \big[W_{n'n\nu}^{(-)}(k, q) + W_{n'n\nu}^{(+)}(k, q) \big], \tag{7}$$

$$\frac{1}{\tau_{kn}^{(\text{inter-op})}} = \frac{2\pi}{N_p \hbar} \sum_{|q| > |q_{\Gamma M}|/2} \sum_{\nu=4}^{9} \sum_{n'} |g_{n'n\nu}(k, q)|^2 \big[W_{n'n\nu}^{(-)}(k, q) + W_{n'n\nu}^{(+)}(k, q) \big], \tag{8}$$

where $|q| = (q_x^2 + q_y^2 + q_z^2)^{1/2}$ and we regard the first three branches from the lowest frequency as acoustic-phonon branches. The summation with respect to q is taken over the first Brillouin zone. For example, $\tau_{kn}^{(\text{intra-ac})}$ can be regarded
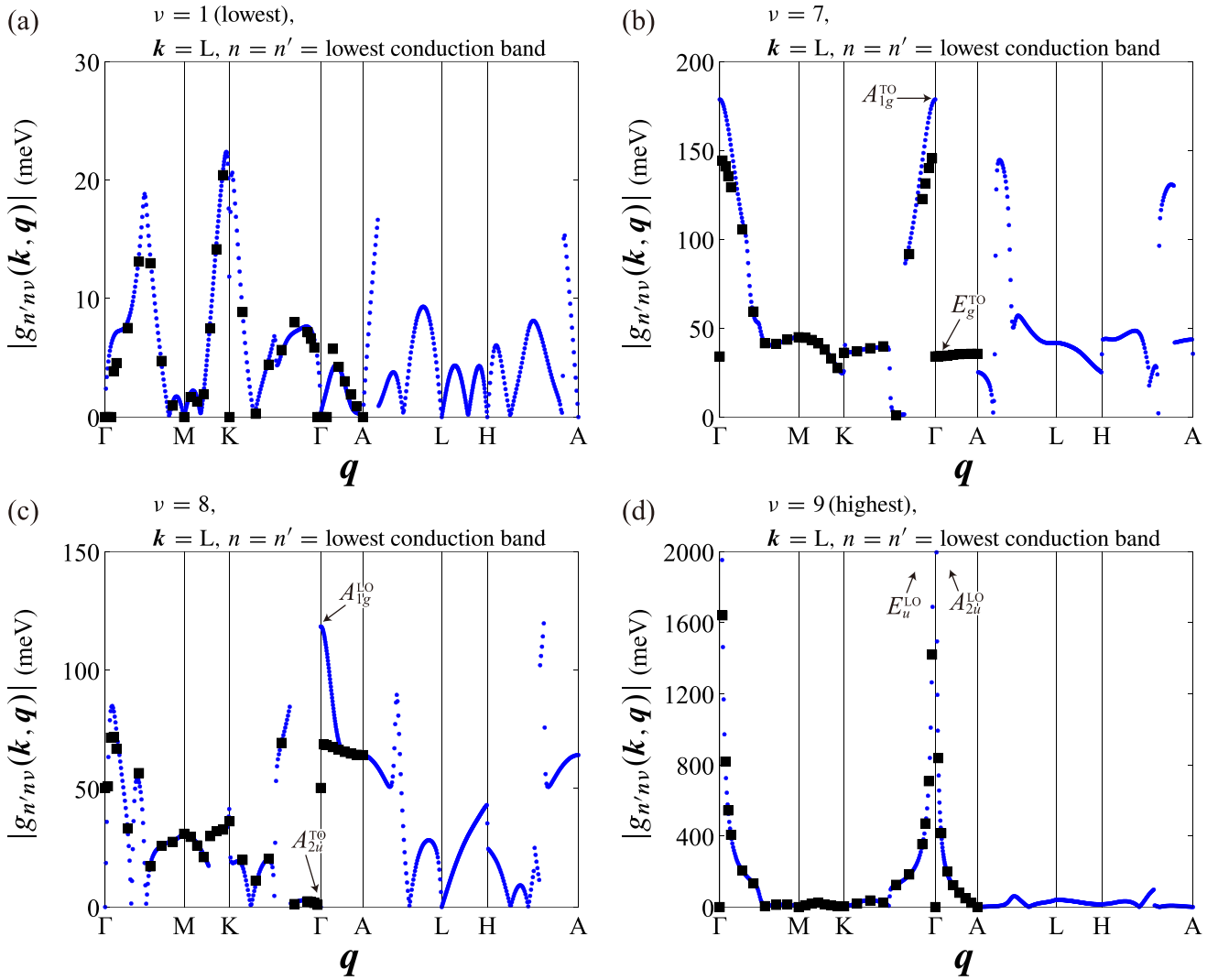
FIG. 2. The q dependence of calculated electron-phonon matrix elements $g_{n'n\nu}(k, q)$ obtained with Wannier interpolations (blue dots) is compared with that of the elements obtained from direct DFPT calculations (black squares). In the calculation of $g_{n'n\nu}(k, q)$, the initial state u_{kn} is set to the bottom of the conduction band at the L point, and the final states $u_{k+qn'}$ are set to the lowest conduction band. The phonon branch ν is set to (a) the first (lowest), (b) the seventh, (c) the eighth, and (d) the ninth (highest). The electron-phonon matrix elements from direct DFPT calculations were obtained only along Γ-M-K-Γ-A. Mulliken symbols [108] are shown for the $q \to 0$ optical modes in (b)–(d).

as the contribution of the intravalley scattering by acoustic phonons to the relaxation time. Since the distance between the centers of the nearest Fermi surfaces is equal to the distance between the Γ and M points, i.e., $|q_{\Gamma M}|$, the scattering processes with $q \leqslant |q_{\Gamma M}|/2$ can be regarded as intravalley scattering as shown in Fig. 1(e). By using the relaxation times $\tau_{kn}^{(\text{intra-ac})}$, $\tau_{kn}^{(\text{intra-op})}$, $\tau_{kn}^{(\text{inter-ac})}$, and $\tau_{kn}^{(\text{inter-op})}$, instead of the total relaxation time τ_{kn} in Eq. (3), we calculated the decomposed resistivities, respectively, and compared them with the total resistivity, which includes all the contributions as shown in Fig. 3(a). We can see that the intravalley scattering processes by optical phonons play a significant role in the resistivity above 80 K. It is apparent that the temperature dependence of the resistivity, which includes all the contributions, is slightly curved, as shown in Fig. 3(a). (See also the logarithmic plots presented in Appendix D.) This behavior mainly comes from the intravalley scattering processes by optical phonons. Similar behavior also has been experimentally observed in

the resistivity of TiS$_2$ [42,44,67,68,73] and in that of ZrSe$_2$ [69–71].

To investigate how the wave vector and frequency dependencies of the electron-phonon matrix elements $g_{n'n\nu}(k, q)$ contribute to the results, we also calculated the resistivity and the decomposed resistivities by substituting a constant value into the electron-phonon matrix elements ($g = 50$ meV) as presented in Fig. 3(b). Comparing this with Fig. 3(a), it is clear that the contribution of the intravalley scattering by optical phonons is vastly underestimated, compared with other kinds of scattering. Thus we can conclude that the large intravalley scattering by optical phonons shown in Fig. 3(a) is due to a large electron-phonon coupling. In fact, we have seen a sharp increase in $|g_{n'n\nu}(k, q)|$ for some optical phonons near $q = 0$ in Fig. 2. We can see that the temperature dependence of the total resistivity by regarding the electron-phonon matrix elements as a constant value is closer to a linear behavior than that obtained with explicit consideration of the matrix
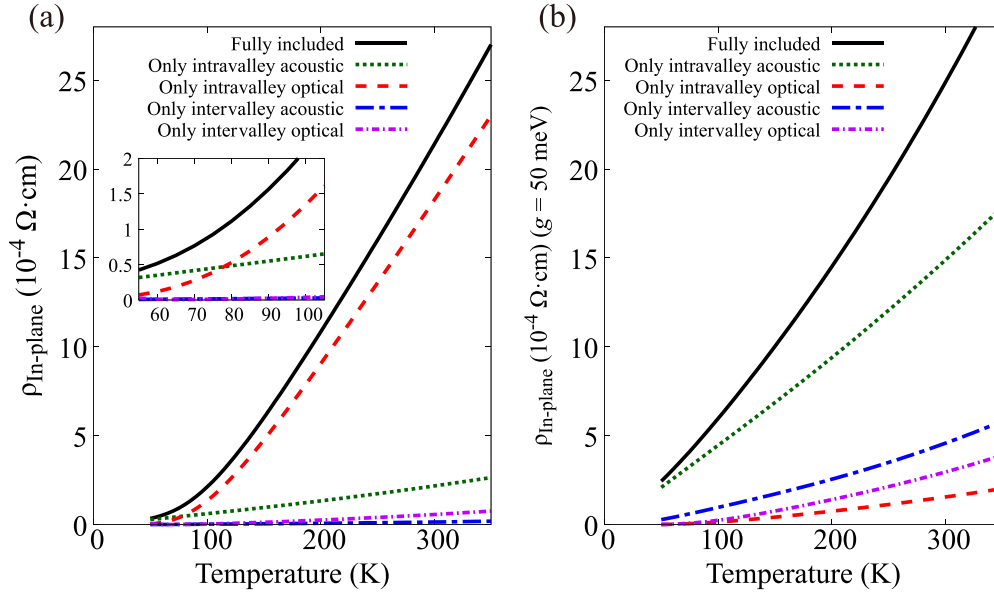
FIG. 3. The temperature dependence of the in-plane electrical resistivity of ZrS_2. The resistivity is calculated (a) with the electron-phonon matrix element obtained from first-principles calculations and (b) with the constant electron-phonon matrix element ($g = 50$ meV). We assumed that the electron carrier density is 1×10^{20} cm^{-3}. The inset in (a) shows a closer view in the lower-temperature region.

elements. Therefore, to understand the temperature dependence of the resistivity, the phonon wave vector and frequency dependence of the electron-phonon matrix elements cannot be ignored.

2. The wavelength- and frequency-resolved resistivity

Using the decomposition of the scattering rate as represented in Eqs. (5)–(8), the temperature dependence of each contribution was obtained, and it was found that the intravalley scattering makes a dominant contribution to resistivity in a wide temperature range. However, since we took partial summations over phonon branches and wave-number vectors, it is difficult to identify the wave-number vectors of phonons that scatter the electrons strongly just from the results shown above. We thus calculated the wavelength- and frequency-resolved resistivity as follows:

$$\rho(q_{\text{cutoff}}, \omega_{\text{cutoff}})$$
$$= \left[\frac{2e^2}{\Omega} \sum_{k,n} \tau_{kn}(q_{\text{cutoff}}, \omega_{\text{cutoff}}) v_{kn}^2 \left(-\frac{\partial f_{kn}}{\partial \varepsilon} \right) \right]^{-1}. \quad (9)$$

We used the following relaxation time, where only the phonon modes satisfying $|q| < q_{\text{cutoff}}$ and $\omega_{qv} < \omega_{\text{cutoff}}$ are taken into account:

$$\tau_{kn}(q_{\text{cutoff}}, \omega_{\text{cutoff}}) = \left[\frac{2\pi}{N_p \hbar} \sum_{n',q,v} |g_{n'nv}(k,q)|^2 \left[W_{n'nv}^{(-)}(k,q) + W_{n'nv}^{(+)}(k,q) \right] \theta(q_{\text{cutoff}} - |q|) \theta(\omega_{\text{cutoff}} - \omega_{qv}) \right]^{-1}, \quad (10)$$

where $\theta(x)$ is the Heaviside step function, whose value is 1 if $x > 0$ and 0 otherwise [110]. We note that $\rho(q_{\text{cutoff}}, \omega_{\text{cutoff}})$ is a monotonically increasing function for q_{cutoff} and ω_{cutoff}; it is equal to the original ρ if q_{cutoff} is greater than the maximum value of the norm of the phonon vector $|q|$, which corresponds to the distance between the Γ and H points $|q_{\Gamma H}|$ in this case, and ω_{cutoff} is greater than the maximum value of the phonon frequency ω_{qv}. One can regard that the phonon states corresponding to $(q_{\text{cutoff}}, \omega_{\text{cutoff}})$ where $\rho(q_{\text{cutoff}}, \omega_{\text{cutoff}})$ changes abruptly make a significant contribution to the electrical resistivity. We thus calculated $\rho(q_{\text{cutoff}}, \omega_{\text{cutoff}})$ and the derivative of $\rho(q_{\text{cutoff}}, \omega_{\text{cutoff}})$, namely, $\partial^2 \rho(q_{\text{cutoff}}, \omega_{\text{cutoff}}) / \partial q_{\text{cutoff}} \partial \omega_{\text{cutoff}}$ for $T = 50$ K and $T = 300$ K as shown in Fig. 4. The derivative $\partial^2 \rho(q_{\text{cutoff}}, \omega_{\text{cutoff}}) / \partial q_{\text{cutoff}} \partial \omega_{\text{cutoff}}$ was calculated

by using the finite-difference method. Figure 4 reveals that the contributions to the resistivity are large within the radius $2k_F$ from the Γ point, where k_F denotes the length of the semimajor axis of the Fermi surface along the A-L line. Thus the strong intensity of $\partial^2 \rho(q_{\text{cutoff}}, \omega_{\text{cutoff}}) / \partial q_{\text{cutoff}} \partial \omega_{\text{cutoff}}$ for $q_{\text{cutoff}} < 2k_F$ in Figs. 4(b) and 4(d) is consistent with the strong intravalley scattering presented in Fig. 3(a). While the acoustic phonons have the dominant contribution at 50 K as shown in Fig. 4(b), the contribution of optical phonons becomes dominant at 300 K as shown in Fig. 4(d). This switching can be naturally understood by the increased occupation of high-frequency phonons at high temperature. We note that, however, as shown in Fig. 3, this switching takes place at around 80 K, which is much lower than the optical phonon frequencies ~30–40 meV. This is because some

$$T = 50 \text{ K}$$

$$T = 300 \text{ K}$$
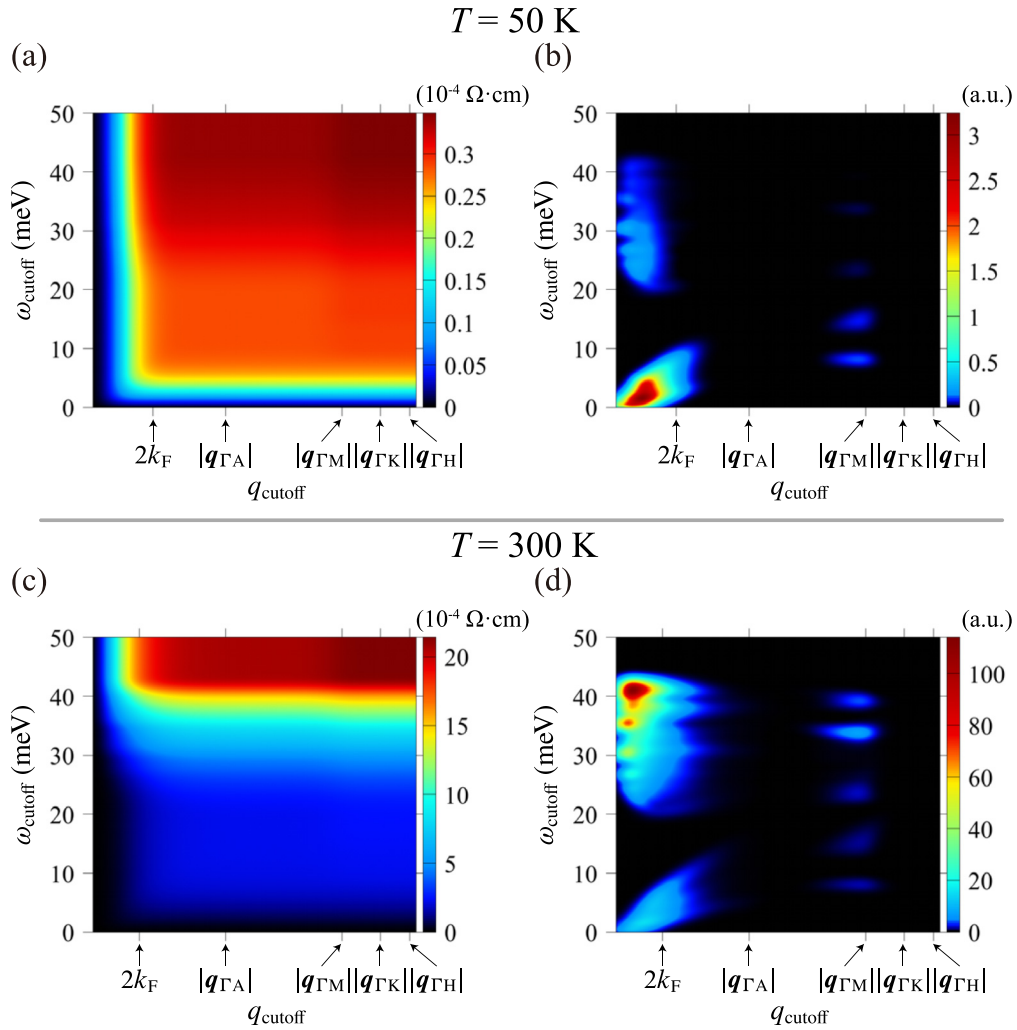
FIG. 4. (a) and (c) The cutoff dependences of the resolved electrical resistivities $\rho(q_{cutoff}, \omega_{cutoff})$ of ZrS$_2$ and (b) and (d) those of their derivatives $\partial^2 \rho(q_{cutoff}, \omega_{cutoff})/\partial q_{cutoff} \partial \omega_{cutoff}$ with an electron carrier density of 1×10^{20} cm^{-3}. (a) and (b) show the cutoff dependences at 50 K, and (c) and (d) show them at 300 K. k_F is defined in the text.

optical phonons bring about strong electron-phonon coupling as we shall discuss in the next paragraph. On the other hand, the intervalley scattering is of less importance because fewer phonons occupy the states near the $q_{\Gamma M}$ points than the states of acoustic phonons at $q \sim 0$, and also the electron-phonon matrix elements coupled with phonons near the $q_{\Gamma M}$ points are not significant.

As mentioned above, the electron-phonon coupling $|g_{n'nv}(\mathbf{k}, \mathbf{q})|$ with some optical phonons becomes quite large around $\mathbf{q} = \mathbf{0}$. In particular, the coupling with polar LO (E_u and A_{2u}) modes diverges in the long-wavelength limit ($\mathbf{q} \to \mathbf{0}$) as shown in Fig. 2(d). Several theoretical studies have also pointed out that the interaction between polar LO phonons and electrons, which was first investigated by Fröhlich [111], plays an important role in the electronic transport also in other polar materials such as bulk GaAs [112–114], mono- or multilayer InSe [115,116], and monolayer MoS$_2$ [84]. Some previous studies also have indicated that the homopolar scattering induced by A_{1g} phonons whose eigenmode corresponds to the vibration of chalcogen layers in counterphase in the direction vertical to the layer plane (so-called "Fivaz"-mode phonons [81]) is the primary scattering mechanism that de-

termines the resistivity of TiS$_2$ [69,78–80] or ZrSe$_2$ [69,70]. Since our calculations do not correctly treat the electron-phonon matrix elements corresponding to the A_{1g} mode as shown in Fig. 2(c), the contribution of the A_{1g} mode to the resistivity cannot be accurately estimated. Therefore we refrain from discussing the scattering caused by the A_{1g} mode phonons in this paper.

Here, we discuss the nonlinear temperature dependence of the resistivity shown in Fig. 3(a). The Bose distribution $n_{qv} = (e^{\beta \hbar \omega_{qv}} - 1)^{-1}$ in Eqs. (3) and (4) can be approximated as $(k_B/\hbar\omega_{qv})T$ if the temperature is higher than the phonon frequency ($\hbar\omega_{qv} < k_B T$), and thus the scattering rate and the resistivity give a linear temperature dependence. When acoustic phonons mainly contribute to the scattering rate, the resistivity shows a linear temperature dependence except in an extremely low temperature range. The linear temperature dependence of the resistivity is often observed in materials whose scattering can be considered to come from acoustic phonons. On the other hand, when optical phonons have a significant contribution, since their frequencies are high, the linear approximation to the Bose factor is not valid even at moderate temperatures, and hence the resistivity can exhibit
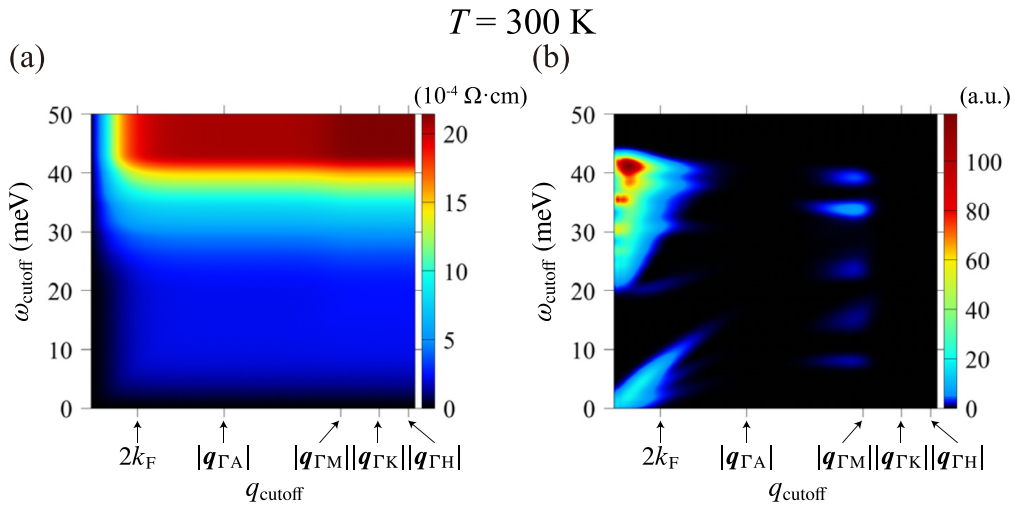
FIG. 5. (a) The cutoff dependence of the resolved electrical resistivity $\rho(q_{cutoff}, \omega_{cutoff})$ of ZrS$_2$ and (b) that of its derivative $\partial^2 \rho(q_{cutoff}, \omega_{cutoff})/\partial q_{cutoff} \partial \omega_{cutoff}$ at 300 K with the electron carrier density of 1×10^{20} cm^{-3}. The wavelength cutoff q_{cutoff} is applied to $(q_x^2 + q_y^2)^{1/2}$ instead of $|\boldsymbol{q}| = (q_x^2 + q_y^2 + q_z^2)^{1/2}$. k_F is defined in the text.

a nonlinear temperature dependence. In fact, in the case of ZrS$_2$, above 80 K (even though the temperature is still several times lower than the frequencies of the E_u and A_{2u} LO phonons and the A_{1g} optical phonons), the optical phonons already play a significant role, and the nonlinear temperature dependence is observed in a wider temperature range. The present analysis may provide an (at least partial) explanation for the nonlinear temperature dependence on the resistivity of TiS$_2$ [42,44,67,68,73] or that of ZrSe$_2$ [69–71]. We note that the RTA, which is symbolized by Eq. (3) and adopted in this paper, can overestimate the forward scattering effects by phonons at $\boldsymbol{q} \sim \boldsymbol{0}$ (and hence the electrical resistivity). This is because when the group velocity of the electrons changes little by the scattering process, it should not significantly affect the

electrical current, while this effect is not taken into account within the RTA. This problem can become significant when the size of the Fermi surfaces, limiting the size of $\boldsymbol{q}$ required to change the direction of the electron group velocity, is much larger than wave vectors of phonons that mainly scatter the electrons. However, in our calculation, the scale of scattering vectors is the same length as the size of the Fermi surface ($\sim 2k_F$) as shown in Fig. 4. Therefore we can regard that the velocity of the electrons changes its direction by intravalley scattering.

Since we discuss the in-plane electrical resistivity in the layered compound, we also calculated the wavelength- and frequency-resolved resistivity $\tilde{\rho}(q_{cutoff}, \omega_{cutoff})$ with the following relaxation time:

$$\tilde{\tau}_{kn}(q_{cutoff}, \omega_{cutoff}) = \left[\frac{2\pi}{N_p \hbar} \sum_{n', \boldsymbol{q}, \nu} |g_{n'n\nu}(\boldsymbol{k}, \boldsymbol{q})|^2 \big[W_{n'n\nu}^{(-)}(\boldsymbol{k}, \boldsymbol{q}) + W_{n'n\nu}^{(+)}(\boldsymbol{k}, \boldsymbol{q}) \big] \theta \Big(q_{cutoff} - \sqrt{q_x^2 + q_y^2} \Big) \theta(\omega_{cutoff} - \omega_{q\nu}) \right]^{-1}, \quad (11)$$

where all the q_z are considered but the q_{cutoff} is applied to $\sqrt{q_x^2 + q_y^2}$. Comparing Figs. 5(a) and 5(b) with Figs. 4(c) and 4(d), the results turned out to be almost the same as those calculated with applying q_{cutoff} to $|\boldsymbol{q}| = \sqrt{q_x^2 + q_y^2 + q_z^2}$. Therefore we can conclude that it is acceptable to compare $|\boldsymbol{q}|$ with $|\boldsymbol{q}_{\Gamma M}|$ and k_F as done in the above discussion, while the $\boldsymbol{q}_{\Gamma M}$ and k_F are defined in the $q_x q_y$ ($k_x k_y$) plane.

B. ZrSe$_2$

We also investigated the electrical resistivity of ZrSe$_2$, which is one of the TMDCs whose electrical resistivity has been measured in previous studies [69–71]. Figure 6 presents the calculated electron and phonon band structures of ZrSe$_2$. Similar to ZrS$_2$, there also exist three Fermi pockets of electrons in the first Brillouin zone. As shown in Fig. 6(b), the

frequencies of optical phonons of ZrSe$_2$ are lower than those of ZrS$_2$.

3. Analysis of the electrical resistivity

To see the effect of the atomic substitution from sulfur atoms to selenium atoms on the resistivity, we calculated the in-plane resistivity of n-type ZrSe$_2$, which is determined from the electron scattering by phonons. For comparison, we also calculated the electrical resistivity using a constant value for the electron-phonon matrix element ($g = 40$ meV) instead of the calculated matrix elements $g_{n'n\nu}(\boldsymbol{k}, \boldsymbol{q})$. Note that the result obtained from the calculated matrix elements is roughly consistent with the experimental value of resistivity, which is 1.25×10^{-2} Ω cm for a Hall carrier concentration of 3.97×10^{19} cm^{-3} at room temperature, reported by Ōnuki *et al.* [69]. As shown in Fig. 7, the nonlinear behavior of the temperature dependence of the resistivity is weakened com-
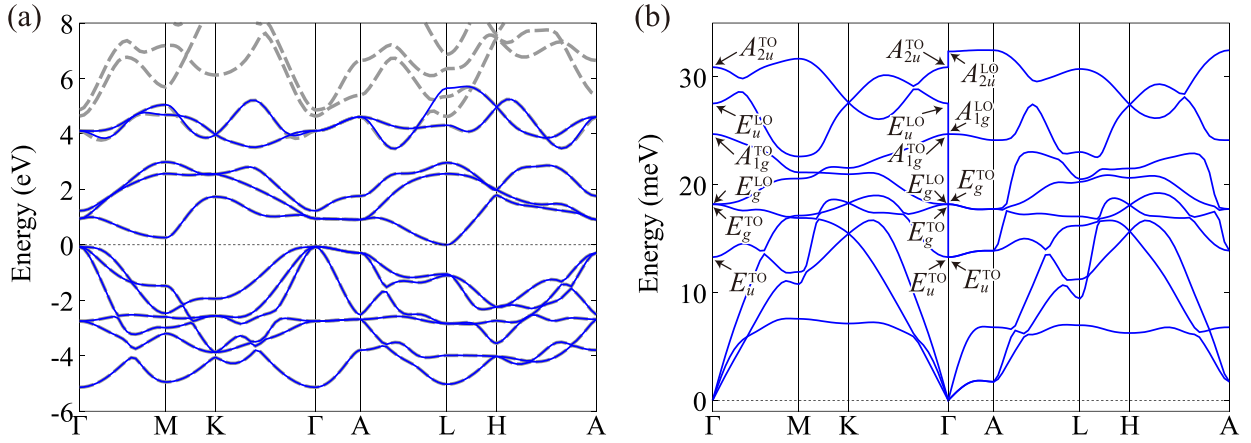
FIG. 6. (a) Electronic band structures of $ZrSe_2$ obtained from first-principles calculations (dashed gray lines) and the effective model constructed by Wannier orbitals (solid blue lines). (b) The phonon dispersion. The optical modes at the Γ point are distinguished by Mulliken symbols [108].

pared with the dependence in ZrS_2 (see also Appendix D); the temperature dependence appears to be almost linear in a wide temperature range. One may expect that a similar analysis as in the case of ZrS_2 can be performed, but the scattering rate of $ZrSe_2$ cannot be decomposed into the contributions coming from acoustic and optical phonons as represented in Eqs. (5)–(8), because the phonon branches of acoustic phonons are entangled with those of optical phonons, as shown in Fig. 6(b). To understand the difference in the temperature dependence of the resistivity between ZrS_2 and $ZrSe_2$, we calculated the wavelength- and frequency-resolved resistivity given by
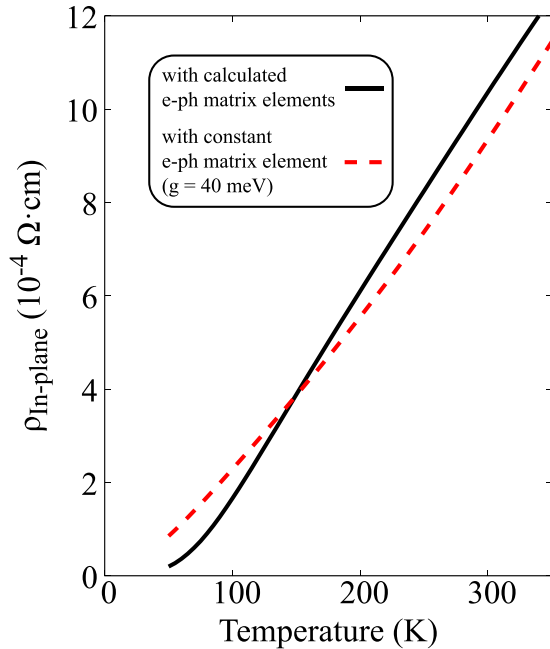
FIG. 7. The temperature dependence of the in-plane electrical resistivity of $ZrSe_2$. The resistivity calculated with the electron-phonon (e-ph) matrix element obtained from first-principles calculations (solid black line) and that calculated with the constant electron-phonon matrix element ($g = 40$ meV) (dashed red line). We assumed that the electron carrier density is 1×10^{20} cm^{-3}.

Eqs. (9) and (10) for 50 and 300 K shown by Fig. 8. First, the difference in the temperature dependence can be understood as follows. The reason for the linearlike temperature dependence in $ZrSe_2$ is that the frequencies of optical phonons decrease compared with those of ZrS_2, and the Bose factor $(e^{\beta \hbar \omega_{qv}} - 1)^{-1}$ can be regarded as $(k_B / \hbar \omega_{qv})T$ in a wider temperature range. Here, we should understand the reason why the value of resistivity is lower than that of ZrS_2. Since the frequencies of the optical phonons become lower, and hence their states are more occupied, one would expect that the resistivity becomes higher. However, the calculated results in Figs. 3 and 8 show the opposite trend. One of the possible reasons is that the electron-phonon matrix elements coupled with the polar LO phonons in $ZrSe_2$ at $\boldsymbol{q} \to \boldsymbol{0}$ are smaller than those in ZrS_2. The divergent behavior of the electron-phonon matrix elements for $\boldsymbol{q} \to \boldsymbol{0}$ depends on the electrostatic potential, which is screened by the electronic permittivity. The in-plane components of dielectric constants ϵ_∞ obtained from the DFPT calculations are 11.99 for ZrS_2 and 18.39 for $ZrSe_2$; the cross-plane components are 5.93 and 9.29, respectively. Therefore it can be considered that the resistivity of $ZrSe_2$ is lower than that of ZrS_2 due to the smaller electron-phonon matrix elements coming from the stronger screening effect on the electrostatic potential.

IV. CONCLUSION

In summary, we have investigated the electron-phonon scattering effect on the resistivity of ZrS_2 and $ZrSe_2$. We have found that the calculated resistivity exhibits a nonlinear temperature behavior, and the tendency is stronger in ZrS_2 than in $ZrSe_2$. According to our analysis of the mode-resolved electrical resistivity, the intravalley scattering by optical phonons mainly contributes to the resistivity at around room temperature. Although optical phonons are less excited than acoustic phonons, the contributions of optical phonons become more extensive than the contributions of the acoustic phonons due to the larger electron-phonon matrix elements coupled with some optical phonons in the higher-temperature range. The intervalley scattering is less significant than the intravalley scattering in both ZrS_2 and $ZrSe_2$. Conversely,

$T = 50$ K

(a)   (b)

$T = 300$ K

(c)   (d)
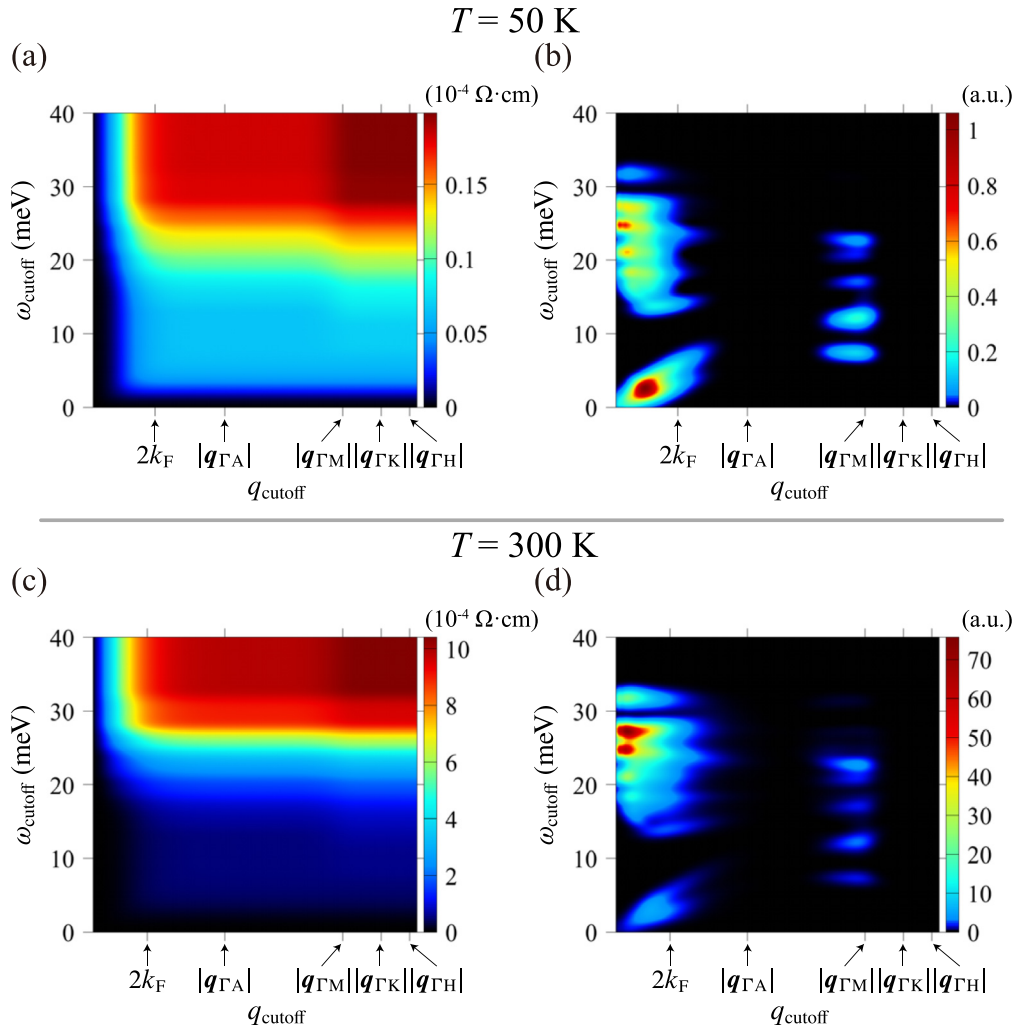
FIG. 8. (a) and (c) The cutoff dependences of the resolved electrical resistivities $\rho(q_{\text{cutoff}}, \omega_{\text{cutoff}})$ of ZrSe$_2$ and (b) and (d) those of their derivatives $\partial^2 \rho(q_{\text{cutoff}}, \omega_{\text{cutoff}})/\partial q_{\text{cutoff}} \partial \omega_{\text{cutoff}}$ with an electron carrier density of 1×10^{20} cm^{-3}. (a) and (b) show the cutoff dependences at 50 K, and (c) and (d) show them at 300 K. The definition of k_F is the same as that for ZrS$_2$, but the value was determined from the size of the Fermi surface of ZrSe$_2$.

the intervalley scattering can have a large contribution to the resistivity if the following conditions are satisfied: (1) The temperature is much lower than the energy scale of optical phonons, but the low-frequency phonon states whose vector connects between electronic valleys are sufficiently occupied, and (2) the electron-phonon matrix elements coupled with optical phonons are not large even at $q \sim \mathbf{0}$. The difference in the temperature dependence of the resistivity between ZrS$_2$ and ZrSe$_2$ can be explained by the difference in the strength of the screening effect on the electron-phonon matrix elements. The present study deepens our understanding of the electron-

phonon scattering effect on the transport properties not only for zirconium dichalcogenides but also for other materials possessing multiple valleys in the electronic band structure.

TABLE I. Optimized crystal structures of ZrS$_2$. Lattice constants: $a = 3.627$ Å, $c = 5.887$ Å.

Element	Multiplicity	Wyckoff letter	Site symmetry	Atomic position
Zr	1	a	$-3m.$	0, 0, 0
S	2	d	$3m.$	1/3, 2/3, 0.2470

TABLE II. Optimized crystal structures of ZrSe$_2$. Lattice constants: $a = 3.724$ Å, $c = 6.116$ Å.

Element	Multiplicity	Wyckoff letter	Site symmetry	Atomic position
Zr	1	a	$-3m.$	0, 0, 0
Se	2	d	$3m.$	1/3, 2/3, 0.2599
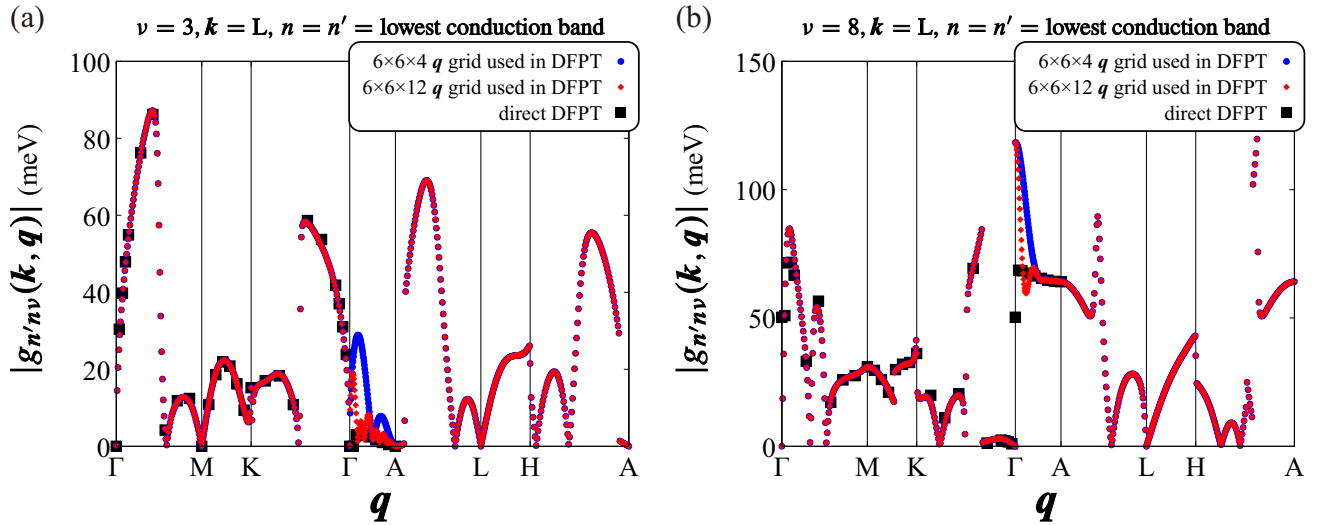
FIG. 9. (a) and (b) The q dependence of calculated electron-phonon matrix elements $g_{n'n\nu}(k, q)$ obtained by Wannier interpolations of the sampling data on the $6\times6\times4$ q grid (blue dots) and on the $6\times6\times12$ q grid (red dots). The electron-phonon matrix elements obtained from direct DFPT calculations are also shown by the black squares. The panels show the q dependence of electron-phonon matrix elements for the two modes, (a) $\nu = 3$ and (b) $\nu = 8$, in which the difference before and after interpolation is noticeable along the Γ-A line.

APPENDIX A: OPTIMIZED CRYSTAL STRUCTURES

Tables I and II present the structural parameters of target materials obtained by our first-principles calculations.

APPENDIX B: CONVERGENCE TESTS

This Appendix provides the results of some convergence tests for the calculations of ZrS$_2$.

1. The sampling q grid used in the DFPT calculations

Figure 2(c) shows that the interpolated matrix elements are not perfectly reproduced by the Wannier interpolation for

some q points. To check the effect of this deviation on the electrical resistivity, we first calculated the electron-phonon matrix elements using different q grids for Wannierization and compared them [117]. The electron-phonon matrix elements interpolated from a $6\times6\times4$ q grid and those from a $6\times6\times12$ q grid are shown in Fig. 9. As shown in Fig. 9, even if we take a finer sampling q grid, we cannot completely get rid of the deviations from the ones obtained by the DFPT calculations around the Γ point. However, we can see that the denser $6\times6\times12$ q grid better reproduces the direct DFPT result. Nevertheless, there is no large difference between the electrical resistivity obtained with the $6\times6\times4$ q-grid sampling and that obtained with the $6\times6\times12$ q-grid sampling as
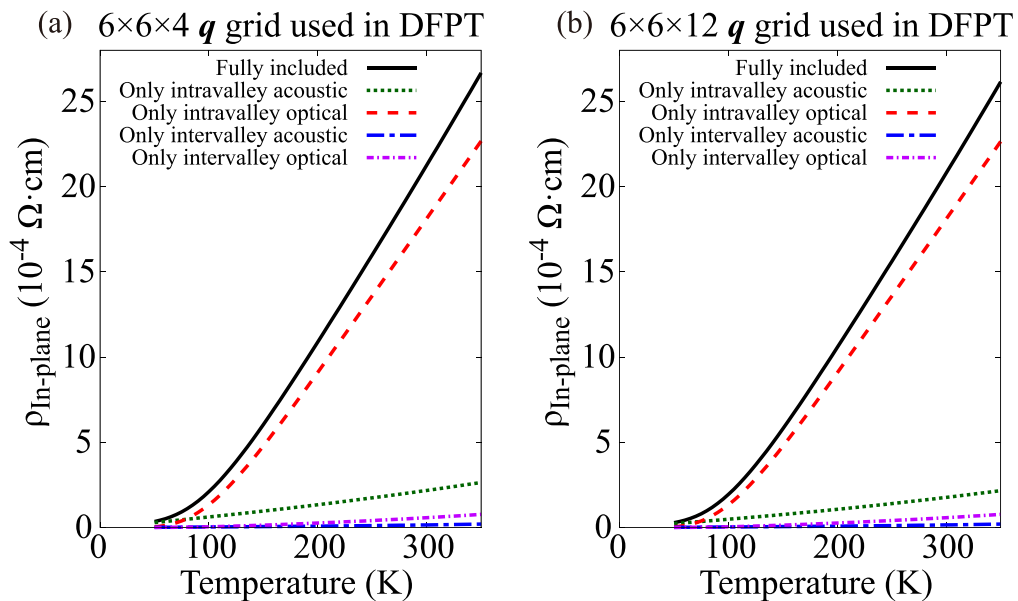
FIG. 10. The temperature dependence of the in-plane electrical resistivity of ZrS$_2$. (a) The data obtained by interpolation with the $6\times6\times4$ q-grid sampling, and (b) the data obtained with the $6\times6\times12$ q-grid sampling.
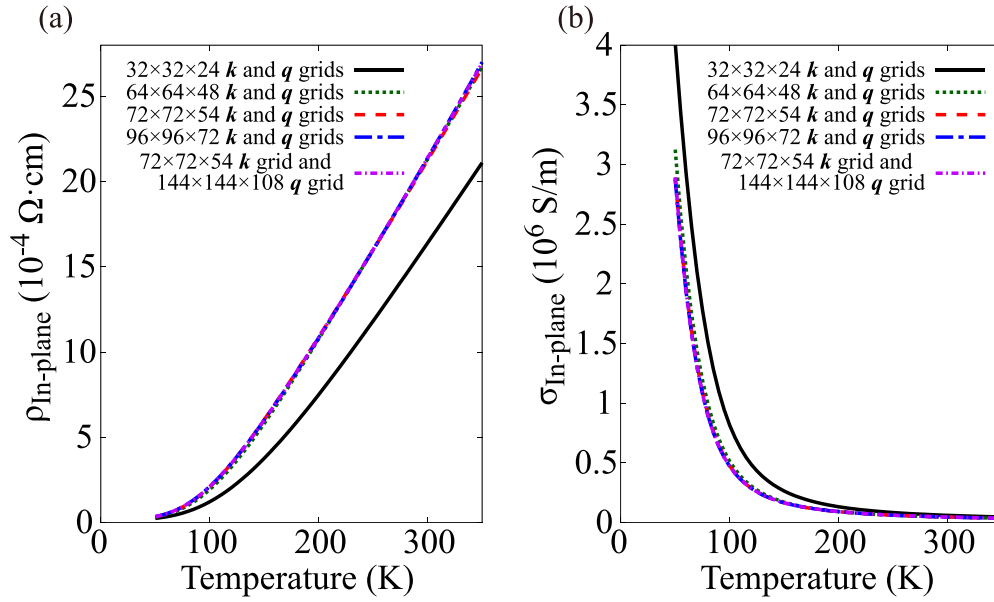
FIG. 11. The temperature dependence of (a) the in-plane electrical resistivity and (b) the in-plane electrical conductivity in ZrS$_2$ with several different grids for calculating the electrical conductivity tensor.

shown in Fig. 10. For both cases, the electrical resistivity was calculated using the $72 \times 72 \times 64$ **k** and **q** grids after Wannier interpolation. The same applies to the electrical conductivity decomposed for each contribution of scattering processes. Therefore we have concluded that the $6 \times 6 \times 4$ **q** grid is sufficient for convergence of the calculation of resistivity, and thus employ it in this paper.

2. The *k* and *q* grids for interpolation

To check carefully what sizes of the **k** and **q** grids for the calculation of Eqs. (1) and (3) are needed to achieve convergence of resistivity, we have calculated the in-plane electrical resistivity and conductivity with some different sizes of grids for interpolation as shown in Fig. 11. The results show that the resistivity calculated even with $64 \times 64 \times 48$ **k** and **q** grids almost achieved convergence. Given these results, we adopt $96 \times 96 \times 72$ **k** and **q** grids in this paper, which are large enough to analyze the resistivity even for the low temperature, ~ 50 K.

APPENDIX C: NORMAL MODES OF LATTICE VIBRATIONS

In the long-wavelength limit $\boldsymbol{q} \to \boldsymbol{0}$, the nine normal vibration modes in ZrS$_2$ and ZrSe$_2$ can be expressed by using the irreducible representations of point group D_{3d} as follows:

$$\Gamma_{\text{vib}} = A_{1g} + E_g + 2A_{2u} + 2E_u, \qquad (\text{C1})$$

where E modes are twofold degenerate. The atomic displacements of each optical mode in the long-wavelength limit are presented in Fig. 12. The electron-phonon matrix elements coupled with the E_u and A_{2u} LO phonons are divergently large

in the long-wavelength limit, as shown in Fig. 2(d), since they macroscopically induce an electric field.

APPENDIX D: DOUBLE LOGARITHMIC PLOTS OF THE ELECTRIC RESISTIVITY AGAINST THE TEMPERATURE

This Appendix includes additional figures to show the temperature dependence of the resistivity in both materials on a logarithmic scale (Fig. 13).
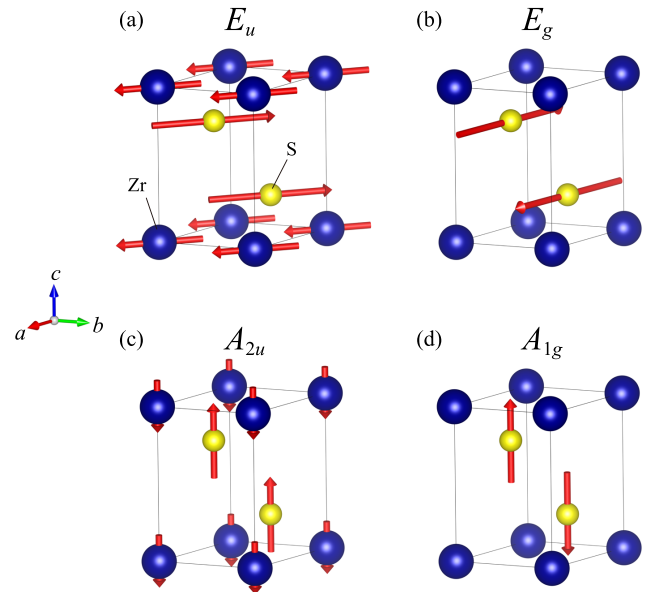
FIG. 12. Atomic displacements in each optical vibration mode of ZrS$_2$. This figure was created using VESTA software [118].
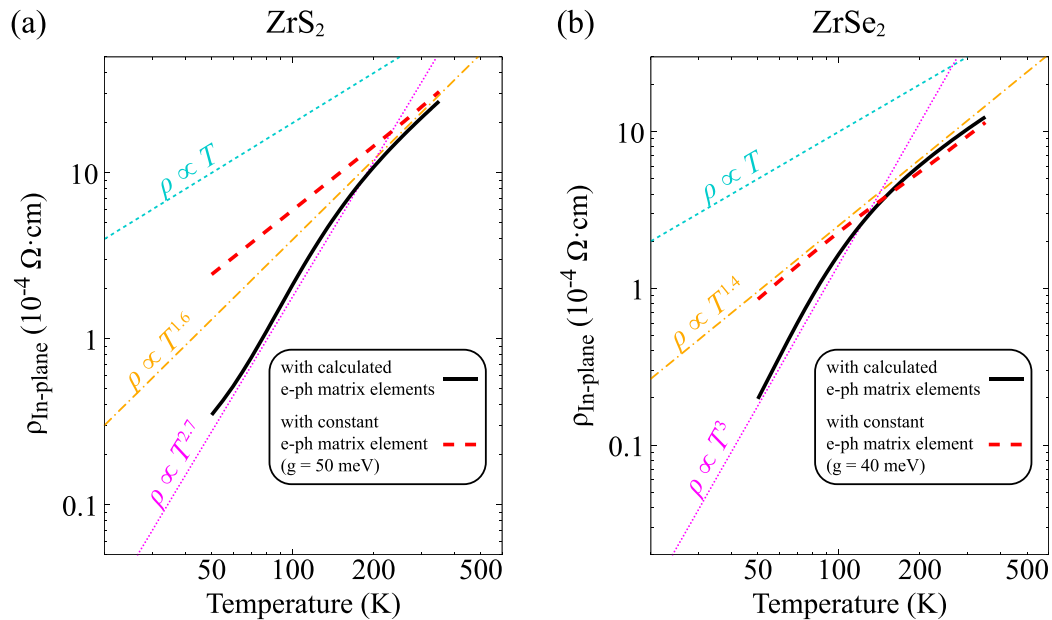
FIG. 13. The temperature dependence of the in-plane electrical resistivity of (a) ZrS_2 and (b) $ZrSe_2$. The logarithmic scale is used for both the vertical and horizontal axes, and some power-law curves are also represented in each panel. The resistivity calculated with the electron-phonon matrix element obtained from first-principles calculations (solid black line) and that calculated with the constant electron-phonon matrix element (dashed red line), which is set as 50 meV for ZrS_2 and 40 meV for $ZrSe_2$. We assumed that the electron carrier density is 1×10^{20} cm^{-3}.

[1] L. F. Mattheiss, Phys. Rev. B **8**, 3719 (1973).

[2] J. A. Wilson and A. D. Yoffe, Adv. Phys. **18**, 193 (1969).

[3] E. Doni and R. Girlanda, in *Electronic Structure and Electronic Transitions in Layered Materials*, edited by V. Grasso (Reidel, Dordrecht, 1986).

[4] Q. H. Wang, K. Kalantar-Zadeh, A. Kis, J. N. Coleman, and M. S. Strano, Nat. Nanotechnol. **7**, 699 (2012).

[5] K. Taniguchi, A. Matsumoto, H. Shimotani, and H. Takagi, Appl. Phys. Lett. **101**, 042603 (2012).

[6] J. T. Ye, Y. J. Zhang, R. Akashi, M. S. Bahramy, R. Arita, and Y. Iwasa, Science **338**, 1193 (2012).

[7] Y. I. Joe, X. M. Chen, P. Ghaemi, K. D. Finkelstein, G. A. de la Peña, Y. Gan, J. C. T. Lee, S. Yuan, J. Geck, G. J. MacDougall, T. C. Chiang, S. L. Cooper, E. Fradkin, and P. Abbamonte, Nat. Phys. **10**, 421 (2014).

[8] C.-X. Liu, Phys. Rev. Lett. **118**, 087001 (2017).

[9] S. C. de la Barrera, M. R. Sinko, D. P. Gopalan, N. Sivadas, K. L. Seyler, K. Watanabe, T. Taniguchi, A. W. Tsen, X. Xu, D. Xiao, and B. M. Hunt, Nat. Commun. **9**, 1427 (2018).

[10] Y. Ma, Y. Dai, M. Guo, C. Niu, Y. Zhu, and B. Huang, ACS Nano **6**, 1695 (2012).

[11] X. Zhu, Y. Guo, H. Cheng, J. Dai, X. An, J. Zhao, K. Tian, S. Wei, X. Cheng Zeng, C. Wu, and Y. Xie, Nat. Commun. **7**, 11210 (2016).

[12] H. Xiang, B. Xu, Y. Xia, J. Yin, and Z. Liu, Sci. Rep. **6**, 39218 (2016).

[13] Y. L. Chiew, M. Miyata, M. Koyano, and Y. Oshima, J. Phys. Soc. Jpn. **89**, 074601 (2020).

[14] F. J. Di Salvo, D. E. Moncton, and J. V. Waszczak, Phys. Rev. B **14**, 4321 (1976).

[15] A. Zunger and A. J. Freeman, Phys. Rev. B **17**, 1839 (1978).

[16] N. Suzuki, A. Yamamoto, and K. Motizuki, J. Phys. Soc. Jpn. **54**, 4668 (1985).

[17] S. Sugai, Phys. Status Solidi B **129**, 13 (1985).

[18] K. Rossnagel, L. Kipp, and M. Skibowski, Phys. Rev. B **65**, 235101 (2002).

[19] T. E. Kidd, T. Miller, M. Y. Chou, and T.-C. Chiang, Phys. Rev. Lett. **88**, 226402 (2002).

[20] F. Clerc, C. Battaglia, H. Cercellier, C. Monney, H. Berger, L. Despont, M. G. Garnier, and P. Aebi, J. Phys.: Condens. Matter **19**, 355002 (2007).

[21] M. Porer, U. Leierseder, J.-M. Ménard, H. Dachraoui, L. Mouchliadis, I. E. Perakis, U. Heinzmann, J. Demsar, K. Rossnagel, and R. Huber, Nat. Mater. **13**, 857 (2014).

[22] K. Dolui and S. Sanvito, Europhys. Lett. **115**, 47001 (2016).

[23] L. J. Li, W. J. Zhao, B. Liu, T. H. Ren, G. Eda, and K. P. Loh, Appl. Phys. Lett. **109**, 141902 (2016).

[24] T. Yu and M. W. Wu, Phys. Rev. B **89**, 205303 (2014).

[25] C. Mai, Y. G. Semenov, A. Barrette, Y. Yu, Z. Jin, L. Cao, K. W. Kim, and K. Gundogdu, Phys. Rev. B **90**, 041414(R) (2014).

[26] S. Dal Conte, F. Bottegoni, E. A. A. Pogna, D. De Fazio, S. Ambrogio, I. Bargigia, C. D'Andrea, A. Lombardo, M. Bruna, F. Ciccacci, A. C. Ferrari, G. Cerullo, and M. Finazzi, Phys. Rev. B **92**, 235425 (2015).

[27] G. Wang, X. Marie, B. L. Liu, T. Amand, C. Robert, F. Cadiz, P. Renucci, and B. Urbaszek, Phys. Rev. Lett. **117**, 187401 (2016).

[28] K. Hao, G. Moody, F. Wu, C. K. Dass, L. Xu, C.-H. Chen, L. Sun, M.-Y. Li, L.-J. Li, A. H. MacDonald, and X. Li, Nat. Phys. **12**, 677 (2016).

[29] P. Rivera, H. Yu, K. L. Seyler, N. P. Wilson, W. Yao, and X. Xu, Nat. Nanotechnol. **13**, 1004 (2018).

[30] G. Wang, A. Chernikov, M. M. Glazov, T. F. Heinz, X. Marie, T. Amand, and B. Urbaszek, Rev. Mod. Phys. **90**, 021001 (2018).

[31] F. Y. Bruno, A. Tamai, Q. S. Wu, I. Cucchi, C. Barreteau, A. de la Torre, S. McKeown Walker, S. Riccò, Z. Wang, T. K. Kim, M. Hoesch, M. Shi, N. C. Plumb, E. Giannini, A. A. Soluyanov, and F. Baumberger, Phys. Rev. B **94**, 121112(R) (2016).

[32] H. Huang, S. Zhou, and W. Duan, Phys. Rev. B **94**, 121117(R) (2016).

[33] L. Huang, T. M. McCormick, M. Ochi, Z. Zhao, M.-T. Suzuki, R. Arita, Y. Wu, D. Mou, H. Cao, J. Yan, N. Trivedi, and A. Kaminski, Nat. Mater. **15**, 1155 (2016).

[34] I. Belopolski, D. S. Sanchez, Y. Ishida, X. Pan, P. Yu, S.-Y. Xu, G. Chang, T.-R. Chang, H. Zheng, N. Alidoust, G. Bian, M. Neupane, S.-M. Huang, C.-C. Lee, Y. Song, H. Bu, G. Wang, S. Li, G. Eda, H.-T. Jeng *et al.*, Nat. Commun. **7**, 13643 (2016).

[35] C. Wang, Y. Zhang, J. Huang, S. Nie, G. Liu, A. Liang, Y. Zhang, B. Shen, J. Liu, C. Hu, Y. Ding, D. Liu, Y. Hu, S. He, L. Zhao, L. Yu, J. Hu, J. Wei, Z. Mao, Y. Shi *et al.*, Phys. Rev. B **94**, 241119(R) (2016).

[36] J. Jiang, Z. K. Liu, Y. Sun, H. F. Yang, C. R. Rajamathi, Y. P. Qi, L. X. Yang, C. Chen, H. Peng, C.-C. Hwang, S. Z. Sun, S.-K. Mo, I. Vobornik, J. Fujii, S. S. P. Parkin, C. Felser, B. H. Yan, and Y. L. Chen, Nat. Commun. **8**, 13973 (2017).

[37] M. Yan, H. Huang, K. Zhang, E. Wang, W. Yao, K. Deng, G. Wan, H. Zhang, M. Arita, H. Yang, Z. Sun, H. Yao, Y. Wu, S. Fan, W. Duan, and S. Zhou, Nat. Commun. **8**, 257 (2017).

[38] K. Zhang, M. Yan, H. Zhang, H. Huang, M. Arita, Z. Sun, W. Duan, Y. Wu, and S. Zhou, Phys. Rev. B **96**, 125102 (2017).

[39] P. Li, Y. Wen, X. He, Q. Zhang, C. Xia, Z.-M. Yu, S. A. Yang, Z. Zhu, H. N. Alshareef, and X.-X. Zhang, Nat. Commun. **8**, 2150 (2017).

[40] Z. Wang, B. J. Wieder, J. Li, B. Yan, and B. A. Bernevig, Phys. Rev. Lett. **123**, 186401 (2019).

[41] I. Kar, J. Chatterjee, L. Harnagea, Y. Kushnirenko, A. V. Fedorov, D. Shrivastava, B. Büchner, P. Mahadevan, and S. Thirupathaiah, Phys. Rev. B **101**, 165122 (2020).

[42] M. Koyano, H. Negishi, Y. Ueda, M. Sasaki, and M. Inoue, Phys. Status Solidi B **138**, 357 (1986).

[43] M. Sasaki, M. Koyano, and M. Inoue, J. Appl. Phys. **61**, 2267 (1987).

[44] H. Imai, Y. Shimakawa, and Y. Kubo, Phys. Rev. B **64**, 241104(R) (2001).

[45] E. Guilmeau, Y. Bréard, and A. Maignan, Appl. Phys. Lett. **99**, 052107 (2011).

[46] C. Wan, Y. Wang, N. Wang, and K. Koumoto, Materials **3**, 2606 (2010).

[47] D. Wickramaratne, F. Zahid, and R. K. Lake, J. Chem. Phys. **140**, 124710 (2014).

[48] A. Samanta, T. Pandey, and A. K. Singh, Phys. Rev. B **90**, 174301 (2014).

[49] C. Bourgès, T. Barbier, G. Guélou, P. Vaqueiro, A. V. Powell, O. I. Lebedev, N. Barrier, Y. Kinemuchi, and E. Guilmeau, J. Eur. Ceram. Soc. **36**, 1183 (2016).

[50] Z. Huang, T. Wu, S. Kong, Q.-L. Meng, W. Zhuang, P. Jiang, and X. Bao, J. Mater. Chem. A **4**, 10159 (2016).

[51] G. Zhang and Y.-W. Zhang, J. Mater. Chem. C **5**, 7684 (2017).

[52] J. R. Schaibley, H. Yu, G. Clark, P. Rivera, J. S. Ross, K. L. Seyler, W. Yao, and X. Xu, Nat. Rev. Mater. **1**, 16055 (2016).

[53] A. Rycerz, J. Tworzydło, and C. W. J. Beenakker, Nat. Phys. **3**, 172 (2007).

[54] D. Xiao, W. Yao, and Q. Niu, Phys. Rev. Lett. **99**, 236809 (2007).

[55] W. Yao, D. Xiao, and Q. Niu, Phys. Rev. B **77**, 235406 (2008).

[56] T. Cao, G. Wang, W. Han, H. Ye, C. Zhu, J. Shi, Q. Niu, P. Tan, E. Wang, B. Liu, and J. Feng, Nat. Commun. **3**, 887 (2012).

[57] K. F. Mak, K. He, J. Shan, and T. F. Heinz, Nat. Nanotechnol. **7**, 494 (2012).

[58] H. Zeng, J. Dai, W. Yao, D. Xiao, and X. Cui, Nat. Nanotechnol. **7**, 490 (2012).

[59] S. Wu, J. S. Ross, G.-B. Liu, G. Aivazian, A. Jones, Z. Fei, W. Zhu, D. Xiao, W. Yao, D. Cobden, and X. Xu, Nat. Phys. **9**, 149 (2013).

[60] H. Yuan, M. S. Bahramy, K. Morimoto, S. Wu, K. Nomura, B.-J. Yang, H. Shimotani, R. Suzuki, M. Toh, C. Kloc, X. Xu, R. Arita, N. Nagaosa, and Y. Iwasa, Nat. Phys. **9**, 563 (2013).

[61] A. M. Jones, H. Yu, N. J. Ghimire, S. Wu, G. Aivazian, J. S. Ross, B. Zhao, J. Yan, D. G. Mandrus, D. Xiao, W. Yao, and X. Xu, Nat. Nanotechnol. **8**, 634 (2013).

[62] K. F. Mak, K. L. McGill, J. Park, and P. L. McEuen, Science **344**, 1489 (2014).

[63] W.-Y. Tong and C.-G. Duan, npj Quantum Mater. **2**, 47 (2017).

[64] Y. Liu, Y. Gao, S. Zhang, J. He, J. Yu, and Z. Liu, Nano Res. **12**, 2695 (2019).

[65] J. A. Benda, Phys. Rev. B **10**, 1409 (1974).

[66] A. H. Thompson, K. R. Pisharody, and R. F. Koehler, Phys. Rev. Lett. **29**, 163 (1972).

[67] A. H. Thompson, Phys. Rev. Lett. **35**, 1786 (1975).

[68] P. C. Klipstein, A. G. Bagnall, W. Y. Liang, E. A. Marseglia, and R. H. Friend, J. Phys. C: Solid State Phys. **14**, 4067 (1981).

[69] Y. Ōnuki, R. Inada, and S.-I. Tanuma, J. Phys. Soc. Jpn. **51**, 1223 (1982).

[70] X.-G. Zheng, H. Kuriyaki, and K. Hirakawa, J. Phys. Soc. Jpn. **58**, 622 (1989).

[71] S. G. Patel, M. K. Agarwal, N. M. Batra, and D. Lakshminarayana, Bull. Mater. Sci. **21**, 213 (1998).

[72] T. Zandt, H. Dwelk, C. Janowitz, and R. Manzke, J. Alloys Compd. **442**, 216 (2007).

[73] D. Suri, V. Siva, S. Joshi, K. Senapati, P. K. Sahoo, S. Varma, and R. S. Patel, J. Phys.: Condens. Matter **29**, 485708 (2017).

[74] C. Herring, Bell Syst. Tech. J. **34**, 237 (1955).

[75] A. Popescu and L. M. Woods, Adv. Funct. Mater. **22**, 3945 (2012).

[76] Y. Pei, H. Wang, and G. J. Snyder, Adv. Mater. **24**, 6125 (2012).

[77] J. Xin, Y. Tang, Y. Liu, X. Zhao, H. Pan, and T. Zhu, npj Quantum Mater. **3**, 9 (2018).

[78] J. A. Wilson, Solid State Commun. **22**, 551 (1977).

[79] J. A. Wilson, Phys. Status Solidi B **86**, 11 (1978).

[80] C. A. Kukkonen, W. J. Kaiser, E. M. Logothetis, B. J. Blumenstock, P. A. Schroeder, S. P. Faile, R. Colella, and J. Gambold, Phys. Rev. B **24**, 1691 (1981).

[81] R. Fivaz and E. Mooser, Phys. Rev. **163**, 743 (1967).

[82] P. F. Maldague and C. A. Kukkonen, Phys. Rev. B **19**, 6172 (1979).

[83] C. A. Kukkonen and P. F. Maldague, Phys. Rev. Lett. **37**, 782 (1976).

[84] K. Kaasbjerg, K. S. Thygesen, and K. W. Jacobsen, Phys. Rev. B **85**, 115317 (2012).

[85] Y. Zhao, Z. Dai, C. Zhang, C. Lian, S. Zeng, G. Li, S. Meng, and J. Ni, New J. Phys. **20**, 043009 (2018).

[86] N. T. Hung, A. R. T. Nugraha, T. Yang, Z. Zhang, and R. Saito, J. Appl. Phys. **125**, 082502 (2019).

[87] T. Sohier, E. Ponomarev, M. Gibertini, H. Berger, N. Marzari, N. Ubrig, and A. F. Morpurgo, Phys. Rev. X **9**, 031019 (2019).

[88] Y. Wu, B. Hou, C. Ma, J. Cao, Y. Chen, Z. Lu, H. Mei, H. Shao, Y. Xu, H. Zhu, Z. Fang, R. Zhang, and H. Zhang, Mater. Horiz. **8**, 1253 (2021).

[89] P. Giannozzi, S. Baroni, N. Bonini, M. Calandra, R. Car, C. Cavazzoni, D. Ceresoli, G. L. Chiarotti, M. Cococcioni, I. Dabo, A. D. Corso, S. de Gironcoli, S. Fabris, G. Fratesi, R. Gebauer, U. Gerstmann, C. Gougoussis, A. Kokalj, M. Lazzeri, L. Martin-Samos *et al.*, J. Phys.: Condens. Matter **21**, 395502 (2009).

[90] P. Giannozzi, O. Andreussi, T. Brumme, O. Bunau, M. B. Nardelli, M. Calandra, R. Car, C. Cavazzoni, D. Ceresoli, M. Cococcioni, N. Colonna, I. Carnimeo, A. D. Corso, S. de Gironcoli, P. Delugas, R. A. DiStasio, A. Ferretti, A. Floris, G. Fratesi, G. Fugallo *et al.*, J. Phys.: Condens. Matter **29**, 465901 (2017).

[91] P. Giannozzi, O. Baseggio, P. Bonfà, D. Brunato, R. Car, I. Carnimeo, C. Cavazzoni, S. de Gironcoli, P. Delugas, F. Ferrari Ruffino, A. Ferretti, N. Marzari, I. Timrov, A. Urru, and S. Baroni, J. Chem. Phys. **152**, 154105 (2020).

[92] L. A. Constantin, J. P. Perdew, and J. M. Pitarke, Phys. Rev. B **79**, 075126 (2009).

[93] J. P. Perdew, A. Ruzsinszky, G. I. Csonka, O. A. Vydrov, G. E. Scuseria, L. A. Constantin, X. Zhou, and K. Burke, Phys. Rev. Lett. **100**, 136406 (2008).

[94] D. R. Hamann, Phys. Rev. B **88**, 085117 (2013).

[95] M. van Setten, M. Giantomassi, E. Bousquet, M. Verstraete, D. Hamann, X. Gonze, and G.-M. Rignanese, Comput. Phys. Commun. **226**, 39 (2018).

[96] N. Marzari and D. Vanderbilt, Phys. Rev. B **56**, 12847 (1997).

[97] F. Giustino, M. L. Cohen, and S. G. Louie, Phys. Rev. B **76**, 165108 (2007).

[98] J. Noffsinger, F. Giustino, B. D. Malone, C.-H. Park, S. G. Louie, and M. L. Cohen, Comput. Phys. Commun. **181**, 2140 (2010).

[99] S. Poncé, E. Margine, C. Verdi, and F. Giustino, Comput. Phys. Commun. **209**, 116 (2016).

[100] S. Poncé, E. R. Margine, and F. Giustino, Phys. Rev. B **97**, 121201(R) (2018).

[101] I. Souza, N. Marzari, and D. Vanderbilt, Phys. Rev. B **65**, 035109 (2001).

[102] A. A. Mostofi, J. R. Yates, Y.-S. Lee, I. Souza, D. Vanderbilt, and N. Marzari, Comput. Phys. Commun. **178**, 685 (2008).

[103] A. A. Mostofi, J. R. Yates, G. Pizzi, Y.-S. Lee, I. Souza, D. Vanderbilt, and N. Marzari, Comput. Phys. Commun. **185**, 2309 (2014).

[104] G. Pizzi, V. Vitale, R. Arita, S. Blügel, F. Freimuth, G. Géranton, M. Gibertini, D. Gresch, C. Johnson, T. Koretsune, J. Ibañez-Azpiroz, H. Lee, J.-M. Lihm, D. Marchand, A. Marrazzo, Y. Mokrousov, J. I. Mustafa, Y. Nohara, Y. Nomura, L. Paulatto *et al.*, J. Phys.: Condens. Matter **32**, 165902 (2020).

[105] R. C. Albers, L. Bohlin, M. Roy, and J. W. Wilkins, Phys. Rev. B **13**, 768 (1976).

[106] D. Wagner and R. Bowers, Adv. Phys. **27**, 651 (1978).

[107] G. Grimvall, *The Electron-Phonon Interaction in Metals* (North-Holland, New York, 1981).

[108] R. S. Mulliken, J. Chem. Phys. **23**, 1997 (1955).

[109] A. Kokalj, J. Mol. Graphics Modell. **17**, 176 (1999).

[110] In actual calculations, we replaced the step function $\theta(x)$ by $[1 + \mathrm{erf}(x)]/2$, where $\mathrm{erf}(x)$ is the Gauss error function.

[111] H. Fröhlich, Adv. Phys. **3**, 325 (1954).

[112] J.-J. Zhou and M. Bernardi, Phys. Rev. B **94**, 201201(R) (2016).

[113] T.-H. Liu, J. Zhou, B. Liao, D. J. Singh, and G. Chen, Phys. Rev. B **95**, 075206 (2017).

[114] J. Ma, A. S. Nissimagoudar, and W. Li, Phys. Rev. B **97**, 045201 (2018).

[115] P. Chang, X. Liu, F. Liu, and G. Du, IEEE Electron Device Lett. **40**, 333 (2019).

[116] L.-B. Shi, S. Cao, M. Yang, Q. You, K.-C. Zhang, Y. Bao, Y.-J. Zhang, Y.-Y. Niu, and P. Qian, J. Phys.: Condens. Matter **32**, 065306 (2020).

[117] Since the EPW code requires that a sampling *q* grid used in the DFPT calculations is commensurate with a sampling *k* grid for Wannierization, we adopted the $12\times12\times12$ sampling *k* grid for Wannierization using the $6\times6\times12$ sampling *q* grid.

[118] K. Momma and F. Izumi, J. Appl. Cryst. **44**, 1272 (2011).